# Scintillation effects and the optimal sequence of deformable mirrors in multi-conjugate adaptive optics

**Marcos A. van Dam**,[a,*] **Bruno Femenía Castellá**,[b,c] **Yolanda Martín Hernando**,[b,c] **Miguel Núñez Cagigal**,[b,c] **Luzma M. Montoya**,[b,c] **and Dirk Schmidt**[d]

[a]Flat Wavefronts, Christchurch, New Zealand
[b]Instituto de Astrofísica de Canarias, La Laguna, Spain
[c]Universidad de La Laguna, Departamento de Astrofísica, La Laguna, Spain
[d]National Solar Observatory, Boulder, Colorado, United States

**Abstract.** Multi-conjugate adaptive optics (MCAO) uses two or more deformable mirrors (DMs) at conjugate altitudes approximately matched to the atmospheric turbulence layers to increase the corrected field of view. An important unresolved problem for MCAO is determining the optimal sequence of the DMs. Theoretical considerations and numerical studies suggest that ordering the DMs from lowest to highest altitude reduces the effects of scintillation, whereas on-sky experiments report that the best performance is attained with the ground-layer DM placed last. Using analytical calculations and numerical experiments with Fresnel propagation of Kolmogorov turbulence, we demonstrate that the scintillation results from spatial frequencies higher than the spatial sampling of high-altitude DMs are able to correct. Hence, the effect of scintillation is not impacted by MCAO correction regardless of the sequence of the DMs. Using end-to-end numerical simulations, we find that the dynamic misregistration between the DMs and the wavefront sensors is minimized by placing the ground-layer DM last, leading to increased loop stability and lower wavefront errors. Contrary to conventional wisdom, we recommend that the DMs be sequenced from highest to lowest altitude.  [DOI: 10.1117/1.JATIS.7.4.049002]

**Keywords:** adaptive optics; multi-conjugate adaptive optics; scintillation; Fresnel propagation; dynamic misregistration.

Paper 21071 received Jul. 4, 2021; accepted for publication Oct. 14, 2021; published online Nov. 2, 2021.

## 1 Introduction

In classical adaptive optics (AO) systems, a single deformable mirror (DM) optically conjugated to the ground corrects for wavefront aberrations caused by atmospheric turbulence. The wavefront correction is best in the direction, in which it is sensed but degrades with increasing angular distance from the guide star, a phenomenon called angular anisoplanatism. It results from the fact that the guide star senses a different portion of the mid- and high-altitude turbulence layers than the science target. Angular anisoplanatism restricts the useful science field of view to between 10 and 30″, depending on science wavelength. At longer wavelengths, the tolerance on wavefront errors is larger and a larger field of view can be used. Propagation of a wave with an aberrated phase to the ground leads to variations in the amplitude of the electric field as well as its phase. The variation in amplitude is known as scintillation and is experienced with the naked eye as the twinkling of stars. While both amplitude and phase variations degrade the image, phase variations dominate the degradation in image quality in astronomical observations.

The corrected science field of view can be expanded by adding one or more additional DMs to correct for mid- and high-altitude turbulence layers in what is known as multi-conjugate adaptive optics (MCAO). MCAO expands the science field of view to typically 30 to 120″, depending on the science wavelength. MCAO has enjoyed some success in night-time

*Address all correspondence to Marcos A. van Dam, marcos@flatwavefronts.com

2329-4124/2021/$28.00 

astronomy, with the multi-conjugate adaptive optics demonstrator[1] at the Very Large Telescope and the Gemini multi-conjugate adaptive optics system (GeMS)[2,3] on Gemini South paving the way. GeMS was designed as a three-DM system but actually uses two DMs because of the failure of one of the DMs. It has been routinely producing corrected near-infrared science images over an $85'' \times 85''$ field since 2013. Solar MCAO has an even longer history.[4–6] The three-DM MCAO system Clear at the Goode Solar Telescope has been providing high-order AO correction over a $30'' \times 30''$ at visible wavelengths since 2016.[7]

A vexing and unresolved issue in the design of the MCAO systems is selecting the sequence, in which the incoming wavefront encounters the DMs. This paper is motivated by the need to decide between competing optical designs for the MCAO system on the European Solar Telescope (EST).[8]

For wide-field optical compensation, Hardy[9] argued using geometric optics considerations that the correct approach is to place the DMs after the focal plane of the telescope and to correct from lowest altitude to highest altitude. Using this sequence of DMs, it is theoretically possible to perfectly cancel the wavefront aberrations. Hardy claimed that inverting the DM sequence "is unsuitable for multiple plane compensation because distortion in the intermediate layers spoils the conjugate imaging" but did not quantify this effect and did not consider scintillation. Flicker was the first to quantify the impact of the DM conjugation order on the Strehl ratio,[10] using an infinite aperture telescope and two DMs that perfectly cancel the wavefront aberrations originating from two discrete turbulence layers. This study concludes that the correcting from lowest to highest layers leads to a relative Strehl ratio improvement of the order of 10% to 15% depending on wavelength and zenith angle. Farley et al.[11] extended the calculations using a finite telescope diameter as well as a large number of turbulent layers and DMs but still assuming perfect compensation of the turbulent layers. The paper concludes that correcting the low-altitude layers first leads to a relative increase in Strehl ratio of up to 15% at 500 nm, with the difference due to increased scintillation.

The altitude layers are imaged by the telescope in the opposite order, from highest to lowest altitude. Reversing the order of the altitude layers requires the inclusion of relay optics between each DM,[9] leading to a reduction in optical throughput and an increase in thermal background, complexity, and cost. For these practical reasons, GeMS and Clear place the DMs in decreasing order of conjugate altitude. Clear deliberately allows the insertion of a ground-layer DM before the other DMs in order to experiment with the DM sequence on-sky.

The DM sequence also affects the performance of the wavefront sensing and control loop, an important point which is not addressed by any of the previous studies. MCAO systems typically employ Shack–Hartmann wavefront sensors optically conjugate to the ground. The registration between the DM actuators and the WFS is calibrated by poking DM actuators and measuring the response of the WFS. Any change in the surface of a high-altitude DM situated between the ground-layer DM and the WFSs leads to a change in registration between the ground-layer DM and the WFSs. Since the optical surface of the high-altitude DM changes with time, this phenomenon is referred to as dynamic misregistration.[12] Dynamic misregistration between every DM but the final one in the sequence and the WFSs will occur regardless of the sequence of the DMs or the conjugate altitude of the WFSs. Dynamic misregistration can lead to loop instability and poor performance.

An on-sky experiment was recently performed using Clear that compared the image quality delivered by the MCAO system with the ground-layer DM placed first with the performance attained with the DM placed last.[13] Measurements of the image contrast as well as the residual wavefront error seen by the WFSs showed a small but Clear advantage to placing the ground-layer DM last, probably due to reduced dynamic misregistration. The role that DM sequence plays in the stability of the control loop is investigated in this paper using numerical simulations for the first time.

This paper reconciles the analytical results with the on-sky experience with Clear. In Sec. 2, we use analytic calculations and computer simulations show that the scintillation is caused predominantly by very high-spatial frequency components of atmospheric turbulence and is largely unaffected by the wavefront compensation afforded by astronomical MCAO. Numerical simulations are presented in Sec. 3 and are used to confirm the analytical results. Section 4 introduces a new end-to-end Monte-Carlo simulation tool that incorporates both the effects of scintillation and the dynamic misregistration. Simulation results produced by this new tool, presented in

Sec. 5, suggest that the optimal performance is obtained with the DMs ordered from highest altitude to lowest, which is in contrast to previous work by others. Conclusions are drawn in Sec. 6.

## 2 Quantifying the Scintillation

In this section, we quantify the effect of scintillation using analytical calculations and numerical simulations of propagated phase screens.

### 2.1 *Atmospheric Parameters*

To quantify the scintillation, we consider the toy problem of an observation at zenith with the Fried parameter $r_0 = 0.08$ m at a wavelength of 500 nm. We adopt a turbulence profile with a vertical distribution of turbulence representative of the EST. The atmospheric parameters used are tabulated in Table 1.

### 2.2 *Analytical Calculations of the Scintillation*

The image quality delivered by an AO system is usually quantified using the Strehl ratio. Consider a wave propagating in the $z$ direction with a complex amplitude of $A\exp[i\phi]$, where $A(x,y)$ is the amplitude and $\phi(x,y)$ is the phase. The extended Maréchal approximation relates the measured Strehl ratio $S$ to the log-amplitude variance $\sigma_\chi^2$ and the phase variance $\sigma_\phi^2$:[14]

$$S \approx \exp[-\sigma_\chi^2]\exp[-\sigma_\phi^2]. \tag{1}$$

The variance of $\chi = \ln A$, the natural logarithm of the amplitude, is used to quantify the scintillation. The log-amplitude variance of a plane wave propagating vertically in the $z$ direction through atmospheric turbulence to the ground is given by[14]

$$\sigma_\chi^2 = 0.2073k_0^2\int \mathrm{d}zC_n^2(z)\int \mathrm{d}\boldsymbol{\kappa}\kappa^{-11/3}\sin^2\left(\frac{\kappa^2 z}{2k_0}\right), \tag{2}$$

where $C_n^2(z)$ quantifies the strength of the turbulence as a function of altitude $z$, $\boldsymbol{\kappa} = (\kappa_x, \kappa_y)$ is the two-dimensional transverse component of the spatial power spectrum, and $\kappa = |\boldsymbol{\kappa}|$ is its amplitude. The value of $k_0$ is related to the wavelength $\lambda$ as

$$k_0 = \frac{2\pi}{\lambda}. \tag{3}$$

Assuming isotropy allows us to replace the angular integration over $d\boldsymbol{\kappa}$ with $2\pi\kappa d\kappa$ yielding

$$\sigma_\chi^2 = 1.3025k_0^2\int_0^\infty dzC_n^2(z)\int_0^\infty d\kappa\kappa^{-8/3}\sin^2\left(\frac{\kappa^2 z}{2k_0}\right). \tag{4}$$

**Table 1** Turbulence profile used in the simulations.

| Elevation (m) | 0 | 1000 | 2000 | 4000 | 8000 | 16,000 |
|---|---|---|---|---|---|---|
| $C_n^2$ ($\times 10^{-14}$ m$^{1/3}$) | 55.4 | 15.1 | 5.0 | 6.0 | 7.1 | 12.1 |
| Turbulence fraction | 0.55 | 0.15 | 0.05 | 0.06 | 0.07 | 0.12 |
| Wind speed (m s$^{-1}$) | 5.6 | 6.25 | 7.57 | 13.31 | 19.06 | 12.14 |
| Wind direction (deg) | 65 | 249 | 194 | 80 | 26 | 239 |

Sasiela[14] showed using Mellin transforms that integrating over $\kappa$ between the limits of 0 and $\infty$ and produced the well-known expression:

$$\sigma_\chi^2 = 0.5631 k_0^{7/6} \int_0^\infty \mathrm{d}z C_n^2(z) z^{5/6}. \tag{5}$$

The log-amplitude variance depends on zenith angle $\zeta$ as $\sigma_\chi^2 \propto \sec^{11/6}(\zeta)$,[14] whereas the uncorrected phase depends on zenith angle as $\sigma_\phi^2 \propto \sec(\zeta)$. The effect of scintillation grows faster with zenith angle than the effect of phase errors.

Both the log-amplitude variance and the phase variance depend on $\lambda$ through the term $k_0$. The phase is related to the almost achromatic wavefront error $w$ as $\phi = k_0 w$. The relationship between log-amplitude variance and wavelength depends on the vertical distribution of turbulence [see Eq. (5)], but it is important to note that $\sigma_\chi^2 \propto \lambda^{-7/6}$ while $\sigma_\phi^2 \propto \lambda^{-2}$. Hence, the reduction in Strehl ratio due to scintillation grows slower with decreasing wavelength than the reduction in Strehl ratio due to wavefront errors. For a given level of wavefront error, the log-amplitude variance relative to the phase variance grows with increasing wavelength.

In AO, the atmosphere is generally modeled as consisting of a modest number $N_L$ of thin layers, so the integral over height is replaced by a summation over the layers. We can approximate the effect of DM correction as an ideal high-pass filter that compensates for low-order turbulence with a wavenumber of $k_a$ or lower ($\kappa \leq k_a$). Let us consider a fictitious band-limited DM with a grid of actuators separated by interactuator spacing $a$. The highest spatial frequency that the DM can create is a sine wave with period $2a$. Hence, the maximum wavenumber that this DM can correct is given by $k_a = 2\pi/(2a) = \pi/a$.

The uncorrected turbulence leads to scintillation that is computed by evaluating the integral in Eq. (2) for wavenumbers between $k_a$ and $\infty$:

$$\sigma_\chi^2(\kappa > k_a) = 1.3025 k_0^2 \sum_1^{N_L} C_n^2(z) \int_{k_a}^\infty \mathrm{d}\kappa \kappa^{-8/3} \sin^2\left(\frac{\kappa^2 z}{2k_0}\right). \tag{6}$$

Numerical evaluations of Eq. (6) as a function of $k_a$ are presented in Sec. 3.

## 3 Numerical Simulations of the Scintillation

Numerical simulations were run to confirm the analytical results using a circular aperture with a 4.2-m diameter, corresponding to the diameter of the EST. Six random atmospheric phase screens with Kolmogorov statistics, one for each turbulent layer, were created using the YAO simulation tool.[15] The $4096 \times 4096$ phase screens spanned 8.4 m $\times$ 8.4 m, with a pixel resolution of 2.05 mm.

To emulate the effect of DM correction, the phase screens were high-pass filtered using the fast Fourier transform (FFT) in the following manner:

1. take the FFT of the phase screen;
2. set the values of the FFT corresponding to $\kappa < k_a$ to zero;
3. take the inverse FFT.

A phase screen used in the simulations is shown in Fig. 1 along with the corresponding high-pass filtered version.

The complex amplitude of the electric field is defined at the top of the atmosphere at a wavelength of 500 nm with uniform amplitude and zero phase. The phase due to the highest altitude layer is added to the electric field and propagated to the next layer using Fresnel propagation. The phase contribution of the second phase screen is added to the complex amplitude and propagated to the third layer. These steps are performed six times to obtain the complex amplitude at the entrance pupil of the 4.2-m diameter EST. We model the telescope as having a circular pupil and no central obscuration or spiders. The Fresnel propagation is performed using the optical propagation tool PROPER described in Sec. 4.[16] The phase screens were translated assuming

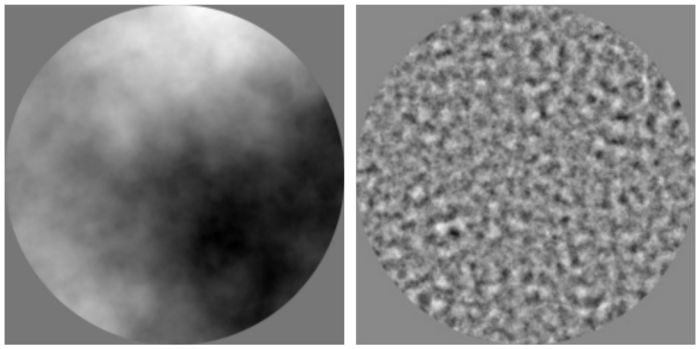


**Fig. 1** (a) Phase screen with Kolmogorov statistics and (b) the output of the high-pass filtering process with a cut-off wavenumber $k_a = 18\,\mathrm{m}^{-1}$.

frozen flow and a time step of 100 ms and the propagation steps repeated. This occurred 100 times for a total integration time of 10 s, long enough for the results to converge. The results of the analytic calculations and numerical simulations are compared in Fig. 2 for the turbulence profile in Table 1. If the integration is performed using Eq. (6) with $k_a = 0$, then the log-amplitude variance is computed to be 0.0611 and simulated to be 0.0652. The small discrepancy between the results two methods is not well understood but is likely to result from incorrect statistics of the low-spatial frequencies of the periodic simulated phase screens. What is most significant is that both curves exhibit excellent agreement in how the log-amplitude variance changes with $k_a$.

Consider an interactuator spacing of 0.175 m corresponding to $k_a$ of $18\,\mathrm{m}^{-1}$ and producing the corrected phase on the right-hand side of Fig. 1. Both curves plotted in Fig. 2 show unambiguously that correcting the spatial frequencies with wavenumbers below $18\,\mathrm{m}^{-1}$ has no effect on the scintillation. This is true even if the DM is conjugated to the same altitude as the turbulence.

Typically, the interactuator spacing of high-altitude DMs is larger than for ground layer DMs for several reasons.

- The high-altitude turbulence is weaker than near the ground (see Table 1).
- The DM altitudes cannot be perfectly matched to the turbulent layers, which change by several kilometers.
- The size of the metapupil (the pupil projected by the entire science field of view at the altitude of the DM) is much larger at high altitudes than near the telescope pupil.

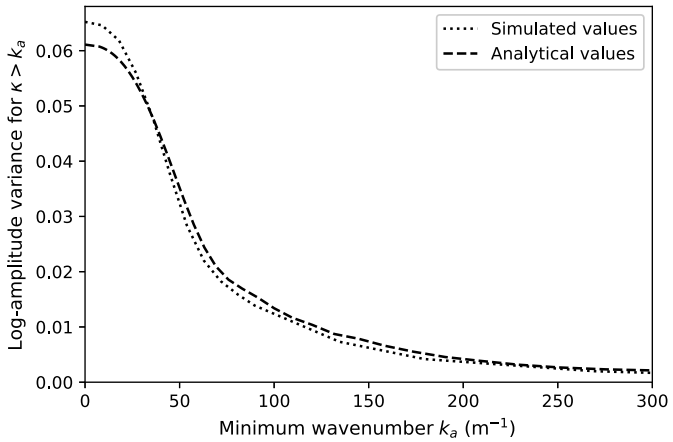


**Fig. 2** Simulated and calculated log-amplitude variance as a function of minimum wavenumber included.

For example, Clear has a high-altitude DM conjugate to 8 km with $a = 0.34$ m, whereas GeMS has a high-altitude DM conjugate to 9 km with $a = 1$ m.

Two lessons can be learned from these results. The first lesson is that the image quality degradation due to scintillation is small even at visible wavelengths, in agreement with previous studies. For the slightly pessimistic atmospheric conditions considered here, the degradation in Strehl is 6% at zenith, rising to 20% at a zenith angle of 60 deg. The second lesson is that wavefront correction has a negligible effect on the scintillation in astronomical AO. Previous studies concluded that applying DM correction from lowest to highest altitude would eliminate scintillation while the opposite DM sequence would double it. Both curves in Fig. 2 clearly show that correcting with a DM with an interactuator spacing of 0.175 m cannot reduce (or increase) the scintillation. Therefore, scintillation should not be a consideration in selecting the DM sequence.

## 4 PropAO: An Extension to the PROPER Optical Propagation Tool

In this section, we present PropAO, the first (to our knowledge) AO simulation tool to model the effect of scintillation and dynamic misregistration. PropAO takes advantage of the optical propagation library PROPER[16] and uses Fresnel propagation to propagate the amplitude and phase of an incoming wave through the atmosphere and through the MCAO system. The resulting wavefront is analyzed by the WFSs and used to calculate the Strehl ratio from the point-spread function (PSF) at the focal plane of the telescope.

The PROPER optical propagation tool, available in IDL, MATLAB, and Python, is a library of routines for optical propagation using physical optics. PropAO uses the Python 3 version of the PROPER as a starting point with a minor but significant change. The calls to NumPY library functions in PROPER are replaced by calls to the same functions in the CuPY library. CuPY translates Python commands into the CUDA programming language to take advantage of the speed of Nvidia graphical processing units, increasing the simulation speed by a factor of 10 to 100 for a high-end laptop.

PROPER has support for pupil stops, DMs, and PSF generation. The remainder of this section describes the additional functionality needed to create an end-to-end AO simulation that is implemented in PropAO. By adopting the simulation architecture of YAO and copying some of its functionality, we can benchmark the behavior and output of PropAO against the output of YAO.

### 4.1 *Atmospheric Turbulence*

PROPER has the capability of inserting amplitude or phase screens anywhere in the optical train but no function to create Kolmogorov phase screens. Atmospheric phase screens were generated using YAO to avoid writing code unnecessarily and to make it easier to compare the results between the two codes. The optical propagation begins at the top of the atmosphere, where the first atmospheric phase screen is inserted. The complex amplitude is propagated to the next atmospheric phase screen, where the phase corresponding to the second atmospheric phase screen is added. This procedure is repeated until we reach the top of the telescope.

### 4.2 *Telescope*

The telescope is modeled as an ideal optical system. The complex amplitude of the incoming wave is multiplied by a circular function that represents the exit pupil of the telescope using a PROPER command. In the future, we could include a realistic optical model of the telescope.

### 4.3 *Deformable Mirrors*

Initially, the native PROPER DM functions were used. However, two limitations drove us to write our own DM module: flexibility and speed. The DM influence function is hard coded in PROPER and loaded as an FITS file. The DM implementation in PROPER was also

prohibitively slow. We wanted to replicate the YAO influence functions initially and then to reproduce the influence functions corresponding to the real DMs.

The DM implementation in PropAO is as follows. The user defines an actuator influence function or can use a preprogrammed one. Current options include the sinc interpolator, the bilinear interpolator, an approximation to the measured influence function of a Xinetics DM, and the same function programmed in YAO. Then the two-dimensional actuator commands are convolved with the influence function to define the surface of the DM. The convolution takes place as a multiplication in the Fourier domain using FFTs. The change in the wavefront is two times the deformation of the surface of the DM.

### 4.4 *Wavefront Sensors*

Shack–Hartmann WFSs are not implemented in PROPER and were implemented in PropAO as follows. The complex amplitude at the pupil plane is subdivided by the lenslet array, and each subaperture is propagated onto the pupil plane to form an image. The centroid of the image produced by each subaperture is computed.

### 4.5 *Wavefront Reconstruction*

The simulations in this paper use a regularized least-squares reconstructor very similar to what is implemented on GeMS at Gemini South and on both telescopes at Keck Observatory.[17] The interaction matrix $H$ is generated by poking the DM actuators one at a time and measuring the response of the WFSs. The reconstructor $R$ is computed as a regularized inverse of the interaction matrix:

$$R = (H^{\mathrm{T}}H + \alpha C_{\phi}^{-1} + P)^{-1}H^{\mathrm{T}}, \tag{7}$$

where $C_{\phi}$ is the covariance matrix of the uncorrected turbulence projected on the DM actuators, $\alpha$ is a regularization constant, and $P$ is a matrix that penalizes piston for each DM. Care must be taken to apply sufficient regularization in the reconstructor (applied by increasing the value of $\alpha$) to avoid instabilities due to dynamic misregistration. However, increasing $\alpha$ beyond its optimal value leads to a reconstruction that is too smooth, resulting in decreased performance.

### 4.6 *Wavefront Control*

The wavefront residual $u$ is obtained by the matrix multiplication of the reconstructor $R$ and the centroids $s$:

$$u = Rs. \tag{8}$$

A leaky integrator with a loop gain $k = 0.4$ and a leak $l = 0.001$ updates the actuator commands at time $n$, $a[n]$ in response to the measured wavefront residual $u[n]$:

$$a[n] = (1 - l)a[n - 1] + ku[n]. \tag{9}$$

Other options for wavefront reconstruction and control, including open-loop control, pseudo-open-loop control, and non-linear iterative reconstructors, have also been implemented.[18] It was shown in van Dam et al. that the pseudo-open-loop control strategy leads to slightly improved performance relative to closed-loop but standard closed-loop control in used in these simulations.

### 4.7 *Science Instrument*

The science instrument is modeled as a simple imager that produces a PSF at an arbitrary wavelength and uses the PSF to estimate the Strehl ratio. A pupil stop may be applied to the science

camera, which was required for the simulations because Clear has a pupil stop in front of the science camera.

## 5 End-to-End Simulations

Simulations were run to emulate the DM sequence experiment performed on-sky using Clear on the Goode Solar Telescope at the Big Bear Solar Observatory,[13] using simulation parameters that replicate the experiment.

### 5.1 *Simulation Parameters*

The Goode Solar Telescope has a telescope diameter of 1.6 m, which is modeled as a circular pupil using 8 mm pixels. The zenith angle was 34 deg and the value of $r_0$ at 500 nm in the observing direction was 0.08 m. Other atmospheric parameters are tabulated in Table 1.

A regular grid of nine wavefront sensing directions taking the values of $-12$, 0, and $12''$ is used to sense the wavefront. The wavefront sensing parameters are tabulated in Table 2.

The experiment on Clear had four DMs with characteristics described in Table 3, with only three DMs used at a time. The interactuator spacing for DM3 matches the size of the WFS subapertures and the location of the actuators corresponds to the corners of the subapertures in what is commonly known as the Fried configuration.[19]

The following DM sequences were compared in simulation:

(A): DM0, DM1, and DM2 at 0, 8000, and 3000 m;
(B): DM1, DM2, and DM3 at 8000, 3000, and 0 m;
(C): DM3, DM2, and DM1 at 0, 3000, and 8000 m;
(D): DM3, DM1, and DM2 at 0, 8000, and 3000 m.

Sequences (A) and (D) correspond to the case where an adaptive secondary mirror is conjugate to the ground, and the remaining DMs are sequenced in the order, in which they are imaged by the telescope. Sequence (B) has the DMs from highest to lowest altitude, whereas sequence (C) has the DMs from lowest to highest altitude.

The reconstructor and control law are described in Secs. 4.5 and 4.6, respectively. The frame rate was 1500 Hz with a loop delay of one cycle. Each simulation consists of a total of 15,000 iterations for an integration time of 10 s, and three sets of simulations were run for each sequence.

**Table 2** Wavefront sensing parameters.

| | |
|---|---|
| Wavelength | 525 nm |
| Subapertures across pupil | 16 |
| Subaperture size | 88 mm |
| Wavefront sensing directions ($''$) | $-12$, 0, 12 |

**Table 3** DM parameters used to simulate the on-sky experiment at Clear. Note that DM3 was actually at 3000 m and not at 4000 m as described by Schmidt et al.[13]

| DM | 0 | 1 | 2 | 3 |
|---|---|---|---|---|
| Altitude (m) | 0 | 8000 | 3000 | 0 |
| Actuators | $19 \times 19$ | $13 \times 13$ | $17 \times 17$ | $17 \times 17$ |
| Actuator pitch (mm) | 80 | 336 | 192 | 88 |

The Strehl ratio was evaluated at the same locations as the WFS but at a wavelength of 656 nm, which corresponds to $H\alpha$. We apply a 1.42-m diameter pupil stop in the science camera to emulate the on-sky experiment.

There are two significant differences between the simulations and the on-sky test by Schmidt et al.[13] First, the WFS used in the simulations is an ideal Shack–Hartmann WFS, where the noiseless centroid of a point source is used to define the wavefront slopes. In the Clear experiment, low-resolution images of a patch of the Sun are correlated against a reference image. Second, Clear uses a modal reconstructor with Karhunen–Loève modes, where the number of modes reconstructed implicitly defines the strength of the regularization. We did not attempt to replicate this reconstructor and used a zonal reconstructor instead.

## 5.2 *Simulation Results*

The experiment on Clear rapidly alternated sequences (A) and (B) while taking narrowband images on the science camera. The seeing was measured with an independent WFS located before the DMs.[13] The image contrast in the central region of the science camera was measured to be higher using sequence (B) than sequence (A) at all three wavelengths recorded in the experiment. For example, the contrast at $H\alpha$ had a median value of 2.4% using sequence (A) and 2.8% with sequence (B).

The simulated average Strehl ratio as a function of position in the field is plotted in Figure 3. The Strehl ratio for sequence (B) is higher than for sequence (A), in agreement with the on-sky experiment. Although it is difficult to translate Strehl ratio into image contrast, it appears that the difference in performance was more significant for Clear than in the simulations.

To understand how statistically significant the results in Fig. 3, the 27 individual Strehl measurements (three simulations and nine positions on the science field) were plotted. Figure 4

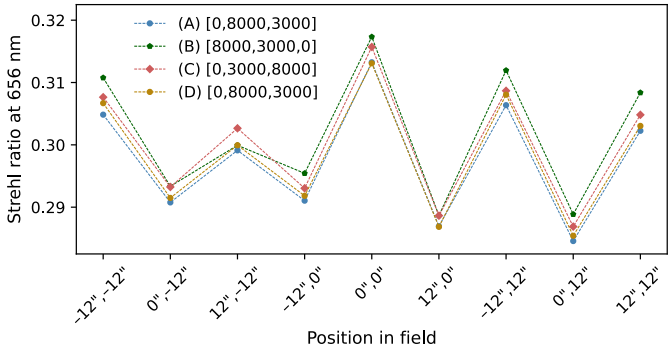


**Fig. 3** Strehl ratio at 656 nm as a function of position in the science field for the four different DM sequences.

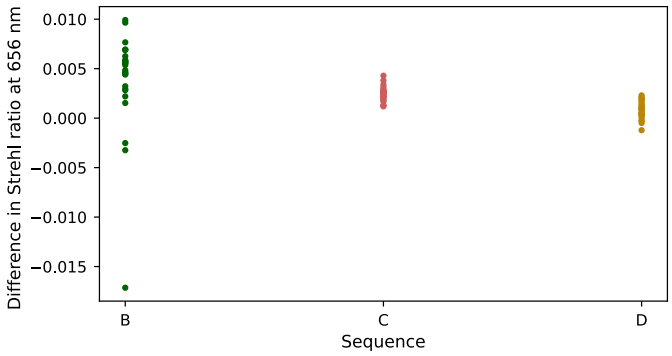


**Fig. 4** Difference in Strehl ratio at 656 nm between sequences (B), (C), and (D) with respect to sequence (A).

**Table 4** Mean and standard deviation of the Strehl ratio at 656 nm over the science field of view.

| Sequence | (A) | (B) | (C) | (D) |
|---|---|---|---|---|
| Strehl ratio | $0.2977 \pm 0.0115$ | $0.3016 \pm 0.0126$ | $0.3001 \pm 0.0117$ | $0.2985 \pm 0.0117$ |

shows the individual results from sequences (B), (C), and (D) with the corresponding result from sequence (A) subtracted. The results from sequence (B) have a larger scatter because sequence (B) is the only sequence with the ground-layer DM last, so the results are less strongly correlated with the results of sequence (A).

The mean and standard deviation of the Strehl ratio across the field are tabulated in Table 4.

The comparison between sequences (A) and (B) for the on-sky experiment is not perfectly fair because the actuator density of the ground-layer DM used in (B) matches the WFS sampling, while the one in (A) is 10% higher. The simulations were also run with mismatched actuator densities. To make the comparison between sequences fair, the simulations were repeated using identical DMs in different orders. Sequence (D) is the same as sequence (A) except that it uses DM3 instead of DM0 as the ground-layer DM to be consistent with sequences (B) and (C). Sequence (C) is the one recommended by Hardy,[9] Flicker,[10] and Farley et al.[11] but produces the lowest Strehl ratio.

The regularization of the reconstructor is increased by increasing the value of $\alpha$ in Eq. (7). Sequence (B) requires the least amount of regularization for a stable control loop, an important factor for on-sky operations where the seeing can change rapidly. This is probably due to the fact that there is no DM between the ground-layer DM and the WFSs to induce dynamic misregistration. Not surprisingly, sequences (A) and (D) require the most regularization, since the DMs are not placed in order of altitude.

The simulation results are very instructive and teach us several lessons. The difference in performance between the different DM sequences is small and probably not sufficiently large to drive the design of the MCAO system. There is no advantage in placing the DMs from lowest to highest altitude, as commonly believed. In fact, placing the DMs from highest to lowest altitude, which is the order in which the layers are imaged by the telescope, produces the highest Strehl ratio, the most stable control loop, and simplest postfocal optical design. Finally, the fact that sequence (D) outperforms sequence (A) indicates that the matching the ground-layer DM actuators to the WFS subapertures is important.

## 6 Conclusion

The DM sequence for astronomical MCAO systems has long been a vexing issue. Previously, theoretical considerations that applied wavefront compensation using geometric optics as well as numerical calculations of scintillation effects suggested that the best performing sequence of DMs is from lowest altitude to highest altitude. In this paper, we calculate analytically and simulate numerically the scintillation effects. We find that the DM sequence has no effect on the scintillation, as previously believed, because the interactuator pitch of the high-altitude DMs is too large to have an impact.

The effect of DM sequence on the performance of the wavefront sensing and control loop also needs to be considered. A new AO simulation tool, which includes the effect of scintillation and dynamic misregistration, is presented and used to replicate an on-sky experiment using Clear on the Goode Solar Telescope. In addition, we compare the performance using three identical DMs but placed in different orders. The simulations show that all DM sequences lead to comparable performance. Sequencing the DMs from lowest to highest altitude does not lead to Strehl ratios that are 10% to 15% higher, as suggested by the literature. On the contrary, the configuration with the DMs sequenced from highest to lowest altitudes produces the highest Strehl ratio and the most stable control loop. Since this configuration is the optically the simplest to implement, it should be preferred for any MCAO system with the postfocal DMs.

## Acknowledgments

This work was supported by the EST Project Office, funded by the Canary Island Government (file SD 17/01) under a direct grant awarded to EST on grounds of public interest. We would like to thank John Krist (JPL) for advice on the use of PROPER and Rodolphe Conan (GMT) for the suggestion to use the CuPY library in place of the NumPY library. The authors have no relevant financial interests in the manuscript and no other potential conflicts of interest to disclose.

## References

1. E. Marchetti et al., "MAD: the ESO multiconjugate adaptive optics demonstrator," *Proc. SPIE* **4839**, 317–328 (2003).
2. F. Rigaut et al., "Gemini multiconjugate adaptive optics system review—I. Design, trade-offs and integration," *Mon. Not. R. Astron. Soc.* **437**(3), 2361–2375 (2014).
3. B. Neichel et al., "Gemini multiconjugate adaptive optics system review—II. Commissioning, operation and overall performance," *Mon. Not. R. Astron. Soc.* **440**(2), 1002–1019 (2014).
4. T. Berkefeld, D. Soltau, and O. von der Lühe, "Results of the multi-conjugate adaptive optics system at the German solar telescope, Tenerife," *Proc. SPIE* **5903**, 59030O (2005).
5. T. Berkefeld, D. Soltau, and O. von der Lühe, "Multi-conjugate solar adaptive optics with the VTT and GREGOR," *Proc. SPIE* **6272**, 627205 (2006).
6. T. Rimmele et al., "Solar multi-conjugate adaptive optics at the Dunn Solar Telescope," in *1st AO4ELT Conf.-Adapt. Opt. for Extremely Large Telesc.*, EDP Sciences, p. 08002 (2010).
7. D. Schmidt et al., "Clear widens the field for observations of the Sun with multi-conjugate adaptive optics," *Astron. Astrophys.* **597**, L8 (2017).
8. T. Berkefeld, "Status of the preparatory work for the 4 m European Solar Telescope," *Proc. SPIE* **10703**, 1070315 (2018).
9. J. W. Hardy, *Adaptive Optics for Astronomical Telescopes*, Oxford University Press (1998).
10. R. C. Flicker, "Sequence of phase correction in multiconjugate adaptive optics," *Opt. Lett.* **26**(22), 1743–1745 (2001).
11. O. Farley et al., "Deformable mirror configuration in MCAO: is propagation a fundamental limit on visible wavelength correction?" in *AO4ELT5* (2017).
12. D. Schmidt et al., "Latest achievements of the MCAO testbed for the GREGOR Solar Telescope," *Proc. SPIE* **7736**, 773607 (2010).
13. D. Schmidt, N. Gorceix, and P. Goode, "On the sequence of deformable mirrors in MCAO: findings from an on-sky, closed-loop experiment," *Proc. SPIE* **11448**, 1144842 (2020).
14. R. J. Sasiela, *Electromagnetic Wave Propagation in Turbulence: Evaluation and Application of Mellin Transforms*, 2nd ed., SPIE Press, Bellingham, Washington (2007).
15. F. Rigaut and M. van Dam, "Simulating astronomical adaptive optics systems using yao," in *AO4ELT3* (2013).
16. J. E. Krist, "PROPER: an optical propagation library for IDL," *Proc. SPIE* **6675**, 66750P (2007).
17. M. A. van Dam, "Wavefront reconstruction and control," in *The WSPC Handbook of Astronomical Instrumentation: Volume 2: UV, Optical & IR Instrumentation: Part 1*, D. N. Burrows, Ed., pp. 205–223, World Scientific (2021).
18. M. A. van Dam et al., "Overcoming the effect of pupil distortion in multiconjugate adaptive optics," *Proc. SPIE* **11448**, 114480P (2020).
19. D. L. Fried, "Least-square fitting a wave-front distortion estimate to an array of phase-difference measurements," *J. Opt. Soc. Am.* **67**(3), 370–375 (1977).

**Marcos A. van Dam** received his BSc and BE (hons.) degrees and his PhD in electrical and electronic engineering all from the University of Canterbury, Christchurch, New Zealand. He is an adaptive optics scientist who runs the adaptive optics company Flat Wavefronts. His research interests span the breadth of adaptive optics disciplines, with a particular interest in wavefront sensing and control.

Biographies of the other authors are not available.